

Cite this: DOI: 10.1039/c8gc03451f

## Defect engineering of nickel hydroxide nanosheets by Ostwald ripening for enhanced selective electrocatalytic alcohol oxidation†

Xianlang Chen,<sup>ID</sup> Xing Zhong,<sup>ID</sup>\* Bowen Yuan, Suiqin Li, Yongbing Gu, Qiaoqiao Zhang, Guilin Zhuang,<sup>ID</sup> Xiaonian Li, Shengwei Deng and Jian-guo Wang<sup>ID</sup>\*

Selective electrocatalytic oxidation (ECO) of alcohols to aldehydes or acids is an environmentally friendly and economical method in modern industries. Herein, tunable holes and vacancies in nickel hydroxide (h-Ni(OH)<sub>2</sub>) by the Ostwald ripening process are successfully fabricated, and the as-prepared electrocatalysts are used for the selective ECO of alcohols into acids or aldehydes with excellent electrocatalytic activity and stability, where a selectivity above 92% to benzoic acid with a benzyl alcohol conversion of 99% on 1.0 h-Ni(OH)<sub>2</sub> was obtained, while a selectivity of >94% to benzaldehyde with a conversion of >90% could also be achieved once the 2,2,6,6-tetramethylpiperidine-*N*-oxyl (TEMPO) radical was employed. A paired electrolysis system is employed using 1.0 h-Ni(OH)<sub>2</sub> and 1.0 PtO<sub>2</sub>/h-Ni(OH)<sub>2</sub> as electrocatalysts at the anode and cathode, respectively, to simultaneously achieve the selective ECO of benzyl alcohol and H<sub>2</sub> production, resulting in a high faradaic efficiency of 192.9%. The excellent ECO activity is mainly due to the abundance of holes and vacancies which facilitate the diffusion rate of the reaction species, adjust the electronic structure and surface properties of h-Ni(OH)<sub>2</sub>, and change the charge density around benzyl alcohol, thereby enhancing the adsorption energy of the alcohol. This study introduces a new avenue for the understanding and future design of advanced defect-based electrocatalysts for electrosynthesis and energy conversion.

Received 5th November 2018,  
Accepted 20th December 2018

DOI: 10.1039/c8gc03451f

rsc.li/greenchem

## Introduction

Selective oxidation of alcohols into the corresponding carbonyl compounds has attracted significant research attention.<sup>1–11</sup> As important industrial chemicals, benzaldehyde and benzoic acid are widely used not only as intermediates in the pharmaceutical and agrochemical industries but also as dyestuffs and food additives.<sup>12–14</sup> Traditional industrial procedures for the synthesis of benzaldehyde and benzoic acid usually involve oxidation of toluene, heating of phthalate anhydride, or hydrolysis of benzyl chloride, all of which not only utilize hazardous or corrosive reagents but also release considerable quantities of undesired by-products.<sup>14–16</sup> Therefore, developing a green and sustainable catalytic oxidation mechanism for benzyl alcohol is highly desirable.<sup>15</sup> Electrocatalytic oxidation (ECO)

is a very promising green process because of its mild reaction conditions and environmental friendliness.<sup>17–22</sup> However, the use of precious metal electrodes (Pt alloy or Pt) or metal-based catalysts entails high costs and metal scarcity during the catalytic process, thereby limiting the development of ECO routes.<sup>23–25</sup> To overcome these drawbacks, Earth-abundant transition-metal compounds, such as (bpy)Cu/2,2,6,6-tetramethyl-1-piperidine-*N*-oxyl (TEMPO) co-catalyst systems or TEMPO derivatives, have been used as catalysts for the ECO of benzyl alcohol.<sup>22,26,27</sup> Besides, three-dimensional Co<sub>3</sub>O<sub>4</sub> NWS/Ti membranes also exhibit outstanding ECO performance for benzyl alcohol, display a high current efficiency toward benzoic acid, and provide an environmentally friendly protocol for the alcohol oxidation processes.<sup>28</sup> To improve the conversion and selectivity of the related reactions, investigating and exploring high-efficiency electrocatalysts with the desired performance is of great significance.

Electrocatalytic activity is closely associated with the availability of active sites.<sup>29</sup> Therefore, maximizing the number of active sites in a catalyst through defect engineering is highly desired to improve its performance in the ECO process. Introducing vacancies and holes to the surface of a catalytic

*Institute of Industrial Catalysis, State Key Laboratory Breeding Base of Green-Chemical Synthesis Technology, College of Chemical Engineering, Zhejiang University of Technology, Hangzhou 310032, P.R. China.*

*E-mail: zhongx@zjut.edu.cn, jgw@zjut.edu.cn*

† Electronic supplementary information (ESI) available: Additional characterization, electrochemical measurement results. See DOI: 10.1039/c8gc03451f

material can effectively adjust its electronic structure and surface properties, increase its active sites, and, thus, remarkably enhance its activity.<sup>30–39</sup> Controlled defect engineering enables the adjustment of the adsorption strength of benzyl alcohol on electrocatalysts, which can affect the conversion and selectivity of ECO. Despite extensive studies on this topic, reports elucidating the influence of holes and vacancies for the ECO of benzyl alcohol are rare. Nickel hydroxide (Ni(OH)<sub>2</sub>)-based materials are well-known and promising electrocatalysts for the oxygen evolution reaction (OER),<sup>40–44</sup> since Ni(OH)<sub>2</sub> can easily facilitate the decomposition of water to form adsorbed OH<sup>−</sup> on its surface in alkaline media.<sup>45–48</sup> Adjusting the surface morphology of the catalyst to modulate the electronic environment of Ni(OH)<sub>2</sub> can influence the adsorption strength of the reactants, and may present a meaningful strategy for the selective ECO of benzyl alcohol.

Based on this concept, herein, we design a facile hydrothermal method combined with Zn etching *via* the Ostwald ripening process to fabricate tunable holes and vacancies on Ni(OH)<sub>2</sub> supported on carbon fiber (CF) to construct 3D nanohybrids (denoted as h-Ni(OH)<sub>2</sub>). The defect structure of the nanohybrid can be modulated by etching with Zn components, thereby providing flexibility to achieve favorable ECO behaviors. The obtained h-Ni(OH)<sub>2</sub> nanohybrid is employed as an anode to investigate its performance for the selective ECO of benzyl alcohols to their corresponding acids or aldehydes. Density functional theory (DFT) calculations indicate that the availability of defects plays a crucial role in modulating the adsorption capability of the catalyst toward the intermediates involved during ECO. Given its unique structural properties, defective h-Ni(OH)<sub>2</sub> exhibits significantly enhanced electrocatalytic activity for the selective ECO of benzyl alcohols.

## Experimental section

### Synthetic procedures

**Pre-treatment of CF.** The commercial carbon fiber (CF) was cut into slices (~2 cm × 4 cm) and ultra-sonicated in HNO<sub>3</sub> (40 wt%), acetone, ethanol and deionized water for 30 min successively. Then the CF was dried at 60 °C for further use. The size (diameter) of the fibers is about 9 μm (Fig. S1†).

**Preparation of h-Ni(OH)<sub>2</sub> on CF.** In a typical preparation, nickel(II) nitrate hexahydrate (25 mmol L<sup>−1</sup>), zinc nitrate hexahydrate, and urea (metal/urea mole ratios of 1:5) were dissolved in 40 mL of deionized water to form a uniform solution by constant stirring. Then the CF and solution were transferred into a Teflon-lined stainless steel autoclave (50 mL), and kept at 120 °C for 12 h. After the autoclave was cooled to room temperature, the CF was ultra-sonicated with deionized water to remove the loosely bound products, and dried at 60 °C under vacuum for 12 h. Finally, the substrate was etched with 5 M NaOH for 24 h, followed by drying at 60 °C under vacuum. Different Ni/Zn mole ratios of 1.5, 1.25, 1.0, 0.75 and 0.5 for the synthesis of 1.5 h-Ni(OH)<sub>2</sub>, 1.25 h-Ni(OH)<sub>2</sub>, 0.75 h-Ni(OH)<sub>2</sub>, 1.0 h-Ni(OH)<sub>2</sub> and 0.5 h-Ni(OH)<sub>2</sub>, which the molar of Ni metal

is fixed. The amount of loading of Ni(OH)<sub>2</sub> is determined by measuring the mass of CF before and after the hydrothermal reaction, which is about 0.625 mg cm<sup>−2</sup>.

**Preparation of 1.0 PtO<sub>2</sub>/h-Ni(OH)<sub>2</sub>.** H<sub>2</sub>PtCl<sub>6</sub>·6H<sub>2</sub>O (5 mg) was dissolved in 40 mL water under vigorous stirring for 30 min. H<sub>2</sub>PtCl<sub>6</sub>·6H<sub>2</sub>O aqueous solution and 1.0 h-Ni(OH)<sub>2</sub> on CF were all transferred into a Teflon-lined stainless steel autoclave (50 mL), and maintained at 373 K for 4 h. After being cooled down to room temperature, 1.0 PtO<sub>2</sub>/h-Ni(OH)<sub>2</sub> was taken out and washed with deionized water thoroughly before being vacuum dried.

**Preparation of h-Cu(OH)<sub>2</sub>, h-Co(OH)<sub>2</sub> and h-Fe(OH)<sub>3</sub> on CF.** The preparation step is similar to that of h-Ni(OH)<sub>2</sub>, except that Co, Cu and Fe nitrates are used instead of nickel nitrate. The loading of the electrocatalysts of h-Fe(OH)<sub>3</sub>, h-Co(OH)<sub>2</sub> and h-Cu(OH)<sub>2</sub> is about 0.600, 0.687 and 0.575 mg cm<sup>−2</sup>, respectively.

**Physicochemical characterization studies.** XRD data were obtained using an XPERT-PRO X-ray diffractometer with Cu Kα (λ = 1.54 Å) radiation. SEM images were obtained with a Hitachi FE-SEM S-4700 at 15 kV. TEM images were obtained with a Tecnai G2F30S-Twin electron microscope operating at an acceleration voltage of 300 kV. EDX mapping and high angle annular dark field-scanning transmission electron microscopy (HAADF-STEM) were performed on a spherical aberration corrected TEM. XPS measurements were performed using a Kratos AXIS Ultra DLD XPS system. Nitrogen adsorption-desorption isotherms were obtained using a Quantachrome NovaWin instrument to measure BET specific surface areas. Atomic force microscopy (AFM) was performed with a Dimension Icon atomic force microscope. CHI 760E and RRDE-3A from ALS were used for CV experiments. A constant current meter was used for ECO. All gas chromatography (GC) experiments were carried out and recorded by GC-MS (Agilent Technologies, HP-5). High performance liquid chromatography (HPLC) was used to analyze products using a C<sub>18</sub> column (4.6 mm × 150 mm) packed with 5 μm diameter particles (Thermo Scientific™ UltiMate™ 3000).

### Electrochemical measurements

**HER and OER.** The HER and OER measurements were performed with a conventional three-electrode system using a CHI 760D (CH Instruments, Inc., Shanghai), with 1.0 h-Ni(OH)<sub>2</sub> on CF (1 × 1 cm<sup>2</sup>) as the working electrode, a graphite rod serving as the counter electrode and Ag/AgCl (in 3 M KCl solution) serving as the reference electrode. The electrochemical HER and OER were performed in H<sub>2</sub>-saturated and O<sub>2</sub>-saturated 1 M KOH solution, respectively.

The potentials were calibrated to a RHE scale using the following equation:

$$E_{(\text{RHE})} = E_{(\text{Ag}/\text{AgCl})} + 0.059 \text{ pH} + 0.197 \quad (1)$$

All the linear sweep voltammetry measurements were *i*R-compensated to account for the voltage drop between the reference and working electrodes. Polarization curves were obtained using LSV with a scan rate of 5 mV s<sup>−1</sup>.

Electrochemical impedance spectroscopy (EIS) measurements were carried out at 1.25 V vs. RHE from 100 kHz to 1 Hz with an amplitude of 5 mV. The values of TOF were calculated according to the following equation:

$$\text{TOF} = \frac{j \times S}{4F \times n} \quad (2)$$

where  $J$  ( $\text{mA cm}^{-2}$ ) is the measured current density at the potentials,  $S$  represents the surface area of the working electrode (1.0 h-Ni(OH)<sub>2</sub> on CF), the number 4 stands for a four-electron transfer per mole of O<sub>2</sub>,  $F$  is Faraday's constant (96 485.3 C mol<sup>-1</sup>), and  $n$  represents the moles of the metal atom on the electrode which can be calculated by using the mass and the molecular weight of the coated catalysts.

**Overall water splitting.** The overall water splitting (OWP) measurement was performed in a paired electrolysis system, in which the 1.0 h-Ni(OH)<sub>2</sub> and 1.0 PtO<sub>2</sub>/h-Ni(OH)<sub>2</sub> electrocatalysts were used as electrodes for the OER and HER, respectively, and linear sweep voltammetry was performed from 1 to 2 V with a scan rate of 5 mV s<sup>-1</sup>.

**ECO of benzyl alcohol.** The ECO of benzyl alcohol was conducted in a two-electrode H-cell system with a cationic Nafion 117 membrane. The anode compartment contained 10 mL of 1 M KOH with 40 mM benzyl alcohol, and 10 mL of 1 M KOH was employed in the cathode compartment. The ECO electrolysis was carried out at room temperature using a constant current of 20 mA until complete consumption of the substrate. 3 mmol% TEMPO was employed in the anode for selective electrocatalytic alcohol oxidation. To analyze the products, 150  $\mu\text{L}$  of the electrolyte solution with 150  $\mu\text{L}$  ethyl acetate was periodically collected during the ECO reaction. The products were analyzed by GC (FuLi GC9790II) to calculate the conversion of benzyl alcohol and selectivity of benzoic acid and benzaldehyde.

The benzyl alcohol conversion (%) and the selectivity (%) of the oxidation products were calculated using eqn (3) and (4):

$$\text{Conversion of benzyl alcohol} = \frac{\text{moles of benzyl alcohol reacted}}{\text{initial moles of benzyl alcohol}} \quad (3)$$

$$\text{Selectivity of oxidation products} = \frac{\text{moles of oxidation products}}{\text{moles of benzyl alcohol reacted}} \quad (4)$$

The faradaic efficiency of benzaldehyde formation was calculated using the equation:

$$\text{Faraday efficiency} = \frac{m \times n \times F}{I \times t} \quad (5)$$

Where  $m$  is the number of moles of the product,  $n$  is the number of electrons obtained from the reactant to the product,  $F$  is Faraday constant (96 485 C mol<sup>-1</sup>),  $I$  is the current, and  $t$  is the time.

### Computational section

Density functional theory (DFT) calculations were performed using the Vienna *ab initio* simulation package (VASP) code with

projector augmented wave (PAW) potentials and the PBE functional for the exchange–correlation energy.<sup>49–54</sup> The kinetic energy cutoff was set to 400 eV. The  $k$ -point meshes were obtained using the Monkhorst–Pack scheme with  $4 \times 4 \times 1$ . In order to simulate the benzyl alcohol adsorbed on vacancy-free Ni(OH)<sub>2</sub> and oxygen defects of Ni(OH)<sub>2</sub> (V<sub>O</sub>-Ni(OH)<sub>2</sub>), the  $4 \times 4 \times 1$  supercell was used for V<sub>O</sub>-Ni(OH)<sub>2</sub> and oxygen defects of Ni(OH)<sub>2</sub>. During the geometry optimizations, all layers were fully relaxed. A vacuum of at least 30 Å was considered along the  $z$  axis. The convergence criteria of the force and energy are 10 meV Å<sup>-1</sup> and 0.01 meV, respectively.

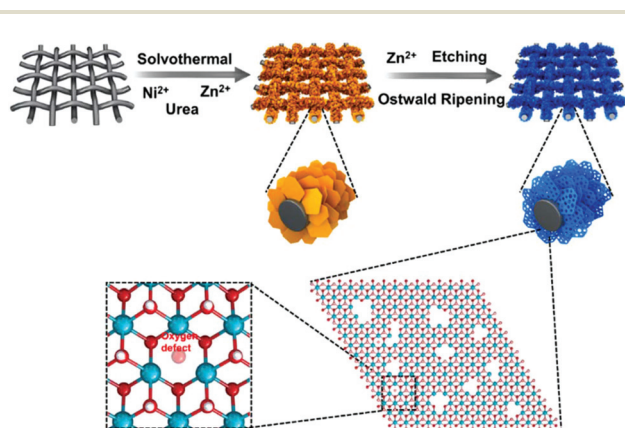
For the DFT calculation of all structures, the adsorption energies ( $E_{\text{ads}}$ ) of benzyl alcohol on vacancy-free Ni(OH)<sub>2</sub> and V<sub>O</sub>-Ni(OH)<sub>2</sub> were calculated by using the equation:

$$E_{\text{ads}} = E_{\text{total}} - E_{\text{adsorbate}} - E_{\text{surf}} \quad (6)$$

where  $E_{\text{total}}$ ,  $E_{\text{surf}}$  and  $E_{\text{adsorbate}}$  are the total energies of the adsorption state system, the total energies of the pure surface and the total energies of benzyl alcohol, respectively.

## Results and discussion

A schematic of the preparation of the h-Ni(OH)<sub>2</sub>/CF electrocatalyst with holes and vacancies is shown in Scheme 1. First, NiZn(OH)<sub>2</sub> arrays were uniformly grown on CF through a facile hydrothermal method in which urea, Zn(NO<sub>3</sub>)<sub>2</sub>, and Ni(NO<sub>3</sub>)<sub>2</sub> are dissolved as raw materials in 40 mL of water. The solution and a piece of clean CF were transferred to a 50 mL Teflon-lined stainless steel autoclave and heated at 120 °C for 12 h. Urea decomposition produces hydroxyl, ammonia, and carbonate, thus providing an alkaline environment in which Ni<sup>2+</sup> and Zn<sup>2+</sup> are precipitated during the hydrothermal reaction to form NiZn(OH)<sub>2</sub> arrays. Then, the as-obtained NiZn(OH)<sub>2</sub>/CF was immersed in 5 M NaOH for 24 h, and the Zn component was selectively removed. Tiny holes and a large number of vacancies were expected to form in h-Ni(OH)<sub>2</sub>/CF, and a transition in the Ni(OH)<sub>2</sub> crystal structure with uniform orientation *via* an *in situ* Ostwald ripening process was observed.<sup>48,55</sup> For



**Scheme 1** Schematic fabrication process of h-Ni(OH)<sub>2</sub>.

comparison, the effects of different Ni/Zn precursor molar ratios were investigated (Experimental section, ESI†).

X-ray diffraction (XRD) was performed to investigate the crystal structure of pristine 1.0 NiZn(OH)<sub>2</sub> and 1.0 h-Ni(OH)<sub>2</sub>. In Fig. 1a, the XRD pattern of 1.0 NiZn(OH)<sub>2</sub> presents five obvious different diffraction peaks that could be attributed to standard  $\alpha$ -Ni(OH)<sub>2</sub> (JCPDS Card No. 380715) and Zn<sub>5</sub>(CO<sub>3</sub>)<sub>2</sub>(OH)<sub>6</sub> (JCPDS Card No. 191458); the peaks at 12.80°, 24.53°, 33.46°, 36.19°, and 59.98° are consistent with the results of previous studies.<sup>56</sup> Compared with 1.0 NiZn(OH)<sub>2</sub>, the diffraction peaks of 1.0 h-Ni(OH)<sub>2</sub> were observed at 19.25°, 33.06°, 38.54°, 52.10°, 59.05°, and 62.72°, respectively, corresponding to the (001), (101), (102), (102), (110), and (111) planes of hexagonal  $\beta$ -Ni(OH)<sub>2</sub> (JCPDS Card No. 140117).<sup>56</sup> No diffraction peaks for Zn<sub>5</sub>(CO<sub>3</sub>)<sub>2</sub>(OH)<sub>6</sub> and  $\alpha$ -Ni(OH)<sub>2</sub> were observed, which demonstrates that Zn<sup>2+</sup> was completely removed from the products and that  $\alpha$ -Ni(OH)<sub>2</sub> was unstable during Ostwald ripening because it is easily transformed into the  $\beta$  phase under alkaline conditions.<sup>47</sup> The diffraction peaks of 0.5, 0.75, 1.25, and 1.5 h-Ni(OH)<sub>2</sub> were identical to those of 1.0 h-Ni(OH)<sub>2</sub> (Fig. S2†). To investigate the structural characterization and morphology of the samples, scanning electron microscopy (SEM) and transmission electron microscopy (TEM) were performed. The SEM images show that 1.0 NiZn(OH)<sub>2</sub> with a network structure was uniformly grown on CF

(Fig. S3†). After Zn removal, the obtained 1.0 h-Ni(OH)<sub>2</sub> turned into porous nanoflakes on CF (Fig. 1b–d). The TEM images of 1.0 h-Ni(OH)<sub>2</sub> and 1.0 NiZn(OH)<sub>2</sub> are shown in Fig. S4.† In Fig. S5–S8,† the SEM images of the as-synthesized h-Ni(OH)<sub>2</sub> electrocatalysts with different Ni/Zn precursor molar ratios before and after Zn removal can be observed. Ostwald ripening occurred during the preferential etching of Zn components, and the dissolved Ni species were redeposited onto the surface of Ni(OH)<sub>2</sub>, resulting in the formation of an abundance of well-distributed holes.<sup>48,57,58</sup> As revealed by the atomic force microscopy (AFM) image in Fig. 1e, the thickness of 1.0 h-Ni(OH)<sub>2</sub> was approximately 12.5 nm. The uniform size distribution of the defects can be observed in Fig. 1f, and the selected area electron diffraction (SAED) pattern shown in the inset in Fig. 1f reveals the crystallinity of h-Ni(OH)<sub>2</sub> with discrete spots. High-resolution TEM (HRTEM) images were obtained for 1.0 h-Ni(OH)<sub>2</sub> (Fig. 1g), and holey defects were found. By contrast, no such defects could be found in 1.0 NiZn(OH)<sub>2</sub> (Fig. S9†). Lattice fringes with a spacing of 0.24 nm could be assigned to the (101) plane of 1.0 h-Ni(OH)<sub>2</sub>, and uniformly distributed holey defects with sizes of about 3–4 nm could be distinctly recognized (Fig. 1g). These findings demonstrate that the selectivity of Zn removal in 1.0 NiZn(OH)<sub>2</sub> induces holey defects, which could help accelerate electrolyte penetration and the release of gas bubbles.<sup>59,60</sup> These features

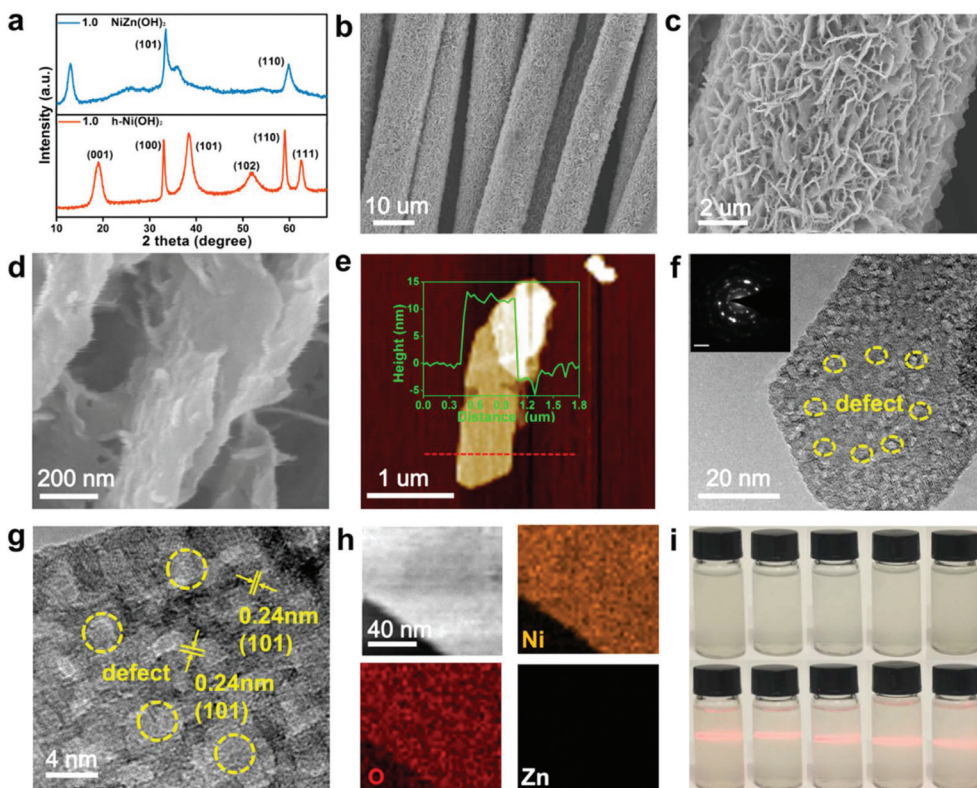


**Fig. 1** (a) XRD results of 1.0 h-Ni(OH)<sub>2</sub> and 1.0 NiZn(OH)<sub>2</sub>. (b–d) SEM images of 1.0 h-Ni(OH)<sub>2</sub>. (e) AFM image of 1.0 h-Ni(OH)<sub>2</sub>. Inset: The corresponding line-scan profile of 1.0 h-Ni(OH)<sub>2</sub>. (f, g) HRTEM images of 1.0 h-Ni(OH)<sub>2</sub>. Inset of (f): The SAED pattern of 1.0 h-Ni(OH)<sub>2</sub>. Scale bar: 5 1 nm<sup>-1</sup>. (h) EDS images of 1.0 h-Ni(OH)<sub>2</sub> showing the homogeneous distribution of Ni and O without Zn. (i) Dispersions of 0.5, 0.75, 1.0, 1.25, and 1.5 h-Ni(OH)<sub>2</sub> (from left to right) in ethanol displaying the Tyndall effect.

are beneficial for the electrocatalytic performance of the obtained nanohybrid. In Fig. S10–S12,† 0.5 h-Ni(OH)<sub>2</sub>, 0.75 h-Ni(OH)<sub>2</sub>, and 1.25 h-Ni(OH)<sub>2</sub> exhibited holey defects similar to those of 1.0 h-Ni(OH)<sub>2</sub>. In addition, the TEM elemental mappings demonstrated the uniform distribution of Ni and O and the insignificant signal of Zn (Fig. 1h), which means that the Zn component could be effectively removed through alkaline etching. The atomic ratio of Ni and O was verified by the corresponding energy dispersive X-ray (EDX) spectrum (Fig. S13†). These results demonstrate that h-Ni(OH)<sub>2</sub> with abundant holey defects was successfully prepared. The porous structure of this material can increase its surface area, thereby providing an abundance of active sites and facilitating mass transport. The Tyndall effect can be observed when an ethanolic suspension of the sample is irradiated with a laser beam (Fig. 1i), which demonstrates the excellent dispersibility and colloidal nature of these h-Ni(OH)<sub>2</sub> samples.

X-ray photoelectron spectroscopy (XPS) characterization studies were conducted to study the valence bond structures of Ni and O in the different samples. Fig. 2a shows the XPS spectra of the as-synthesized h-Ni(OH)<sub>2</sub> samples; the peaks obtained indicate the presence of O and Ni. Fig. 2b shows the Ni 2p XPS spectra of 1.0 NiZn(OH)<sub>2</sub>; here, the peaks at 855.7 and 873.5 eV are attributed to the peaks of Ni 2p<sub>3/2</sub> and Ni 2p<sub>1/2</sub>, respectively. Two satellite peaks located at 861.5 and 879.8 eV are assigned to the same species.<sup>61,62</sup> These four peaks are negatively shifted in 0.5, 0.75, 1.0, 1.25, and 1.5 h-Ni(OH)<sub>2</sub> by

about 0.3 eV compared with those of 1.0 NiZn(OH)<sub>2</sub>, thereby indicating that the Ni content of h-Ni(OH)<sub>2</sub> has a modified local electronic structure, which may be used to approximate the ideal Ni–OH phase.<sup>62,63</sup> The O 1s peak of 1.0 NiZn(OH)<sub>2</sub> is positively shifted by about 0.3 eV, which is in agreement with the results of the Ni 2p spectrum (Fig. 2c). Fig. 2d shows the O 1s XPS of different h-Ni(OH)<sub>2</sub> samples; here, the main peaks of O1, O2, O3, and O4 at 532.3, 531.5, 530.7, and 529.8 eV correspond to surface O–C=O, adsorbed OH, lattice OH, and lattice O, respectively.<sup>64,65</sup> In the O 1s XPS spectrum of 1.0 h-Ni(OH)<sub>2</sub>, the sum of lattice OH and O is distinctly less than that of 1.5 h-Ni(OH)<sub>2</sub>, which indicates the presence of more oxygen vacancies on the surface of 1.0 h-Ni(OH)<sub>2</sub>.<sup>65</sup> Other h-Ni(OH)<sub>2</sub> samples also showed that their sum of relative contents of lattice OH and O was lower than that of 1.5 h-Ni(OH)<sub>2</sub> (Table S1†). These results confirm the presence of oxygen vacancies on the surface of all holey Ni(OH)<sub>2</sub> samples. To determine the specific surface areas of the h-Ni(OH)<sub>2</sub> samples, their N<sub>2</sub> adsorption–desorption isotherms were determined. In Fig. 2e, the plots of the as-synthesized h-Ni(OH)<sub>2</sub> samples show a type-IV isotherm with a hysteresis loop,<sup>66</sup> which indicates a mesoporous size distribution. The Brunauer–Emmett–Teller (BET) specific surface areas of the 0.5, 0.75, 1.0, 1.25, and 1.5 h-Ni(OH)<sub>2</sub> samples are 31.01, 37.94, 63.89, 88.92 and 108.19 m<sup>2</sup> g<sup>−1</sup>, respectively (Table S2†). Differences in the specific surface area of the samples are attributed to differences in their Zn content. The Barrett–Joyner–Halenda (BJH) curves of the pore size distributions of the samples further confirm that the majority of the holes are about 3–4 nm in size (Fig. 2f), which fairly satisfactorily matches the HRTEM results. The unique porous features of h-Ni(OH)<sub>2</sub> can provide numerous channels, promote contact between the catalyst and the electrolyte, and lead to rapid charge and mass transport during electrolysis, all of which are crucial for improving ECO performance.

The electrocatalytic OER activities of h-Ni(OH)<sub>2</sub> were studied to investigate the effect of defects and vacancies on its electrocatalytic performance by using a typical three-electrode device in 1 M KOH aqueous solution. The linear sweep voltammetry (LSV) curves of the samples are shown in Fig. 3a. The polarization curve of all samples shows a peak at around 1.45 V (*versus* that of a reversible hydrogen electrode, RHE), corresponding to the redox reaction of Ni<sup>2+</sup>/Ni<sup>3+</sup>; this result indicates that the electrocatalytically active β-NiOOH phase,<sup>56,67,68</sup> which is vital for the high activity for the OER,<sup>69</sup> is rapidly and substantially formed. The anodic current density increased dramatically under a more positive potential, thus suggesting the excellent OER activity of the electrocatalyst. As seen in Fig. 3a, among those of the other samples, the OER performance of 1.0 h-Ni(OH)<sub>2</sub> is the best. This phenomenon indicates that 1.0 h-Ni(OH)<sub>2</sub> features the optimal number of holes and oxygen vacancies (Fig. 1f and Table S1†). The electrocatalytic ability of the holey Ni(OH)<sub>2</sub> is clearly significantly related to the etched Zn content. The characteristics of Ni-bonding changed successively during the preferential etching of Zn components, creating more active sites around holey defects, causing changes in the local electronic structure, and provid-

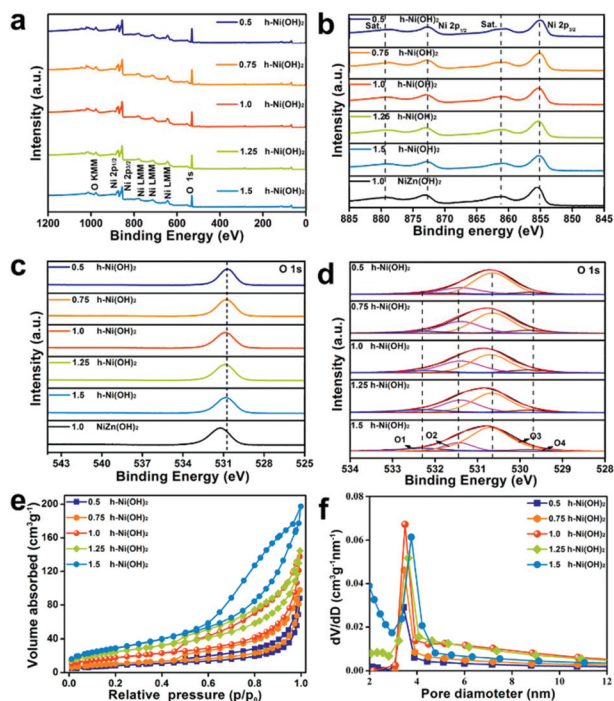


**Fig. 2** (a) XRD spectra of different h-Ni(OH)<sub>2</sub> samples. (b, c) XRD spectra of Ni and O in different h-Ni(OH)<sub>2</sub> samples. (d) O 1s XPS spectra of different h-Ni(OH)<sub>2</sub> samples. (e, f) N<sub>2</sub> adsorption–desorption isotherms and the corresponding BJH pore size distributions of different h-Ni(OH)<sub>2</sub> samples.

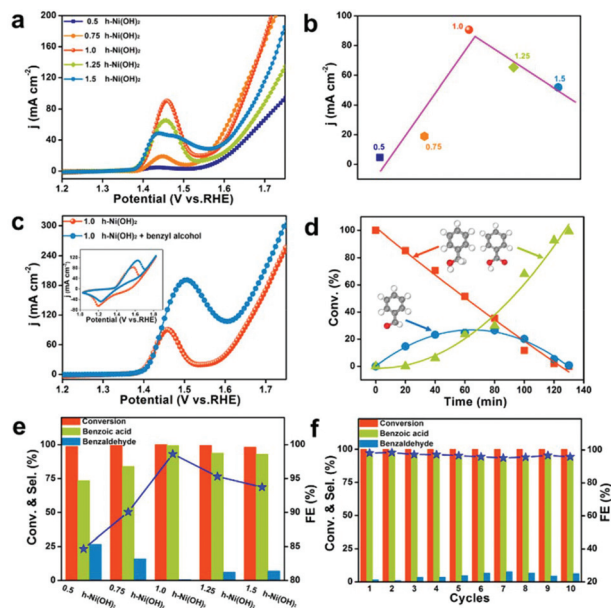


**Fig. 3** (a) OER polarization curves of the different  $\text{h-Ni(OH)}_2$  samples. (b) Highest current density of the redox peaks of different  $\text{h-Ni(OH)}_2$  samples. (c) OER LSV curves of 1.0  $\text{h-Ni(OH)}_2$  in the absence and presence of  $40 \times 10^{-3}$  M benzyl alcohol in 1.0 M KOH. Inset: CV curves. (d) Conversion and selectivity for ECO at a continuous current of 20 mA in  $40 \times 10^{-3}$  M benzyl alcohol with 1.0 M KOH. (e) Conversion, selectivity, and FE obtained from different electrocatalysts. (f) Conversion, selectivity, and FE obtained after 10 reaction cycles using 1.0  $\text{h-Ni(OH)}_2$ .

ing remarkable OER performance. The quasi-reversible oxidation and reduction peaks obtained could be attributed to the conversion from  $\text{Ni(OH)}_2$  to active  $\text{NiOOH}$ , and continuous reduction to  $\text{Ni(OH)}_2$  could be observed in a typical cyclic voltammogram (CV) curve (Fig. S14<sup>†</sup>). Moreover, it is remarkable that 1.0  $\text{h-Ni(OH)}_2$  exhibited a much higher intensity of this oxidation peak with a greater peak area than the other samples, which indicates the substantial and fast transformation from  $\text{Ni(OH)}_2$  to the more active  $\text{NiOOH}$ . The highest oxidation peak values acquired from the electrocatalysts with different Ni/Zn ratios showed a volcano plot (Fig. 3b). The electrocatalytic kinetics were supported by the Tafel slopes obtained. The Tafel slope of 1.0 holey  $\text{Ni(OH)}_2$ , at  $114 \text{ mV dec}^{-1}$  (Fig. S15<sup>†</sup>), is the lowest among those of 0.5  $\text{h-Ni(OH)}_2$  ( $255 \text{ mV dec}^{-1}$ ), 0.75  $\text{h-Ni(OH)}_2$  ( $160 \text{ mV dec}^{-1}$ ), 1.25  $\text{h-Ni(OH)}_2$  ( $158 \text{ mV dec}^{-1}$ ), and 1.5  $\text{h-Ni(OH)}_2$  ( $189 \text{ mV dec}^{-1}$ ). This result demonstrates the rapid OER kinetics of 1.0  $\text{h-Ni(OH)}_2$ . The outstanding performance of this catalyst was proven by the electrochemical impedance spectroscopy (EIS) data. The charge transfer resistance of 1.0  $\text{h-Ni(OH)}_2$  was much lower than those of the other as-synthesized  $\text{h-Ni(OH)}_2$  electrocatalysts (Fig. S16<sup>†</sup>) because the abundance of holes and oxygen vacancies in the former facilitates charge transfer. Furthermore, Fig. S17<sup>†</sup> shows the turnover frequency (TOF) estimation. At the highest anodic oxidation peak of  $90.67 \text{ mV cm}^{-2}$ , the TOF of 1.0  $\text{h-Ni(OH)}_2$  is  $127 \text{ h}^{-1}$ , which is 20, 4.85, 1.42, and 1.76 times higher than those of

0.5  $\text{h-Ni(OH)}_2$ , 0.75  $\text{h-Ni(OH)}_2$ , 1.25  $\text{h-Ni(OH)}_2$ , and 1.5  $\text{h-Ni(OH)}_2$ , respectively; this result further demonstrates the outstanding activity of the 1.0  $\text{h-Ni(OH)}_2$  electrocatalyst for the OER. As can be seen from Fig. S18<sup>†</sup>, the current density of 1.0  $\text{h-Ni(OH)}_2$  exhibits no noticeable degradation after 10 h of continuous OER operation. The TEM images of 1.0  $\text{h-Ni(OH)}_2$  after the OER demonstrate that the hole defects are maintained (Fig. S19<sup>†</sup>). These results prove that holes and oxygen vacancies in the catalyst can improve its charge-transfer capability and electrical conductivity and provide specific active sites, thereby improving its electrocatalytic activity and stability.

Based on the OER results, the electrocatalytic properties of the hybrids for the ECO of benzyl alcohol were evaluated. The LSV of 1.0  $\text{h-Ni(OH)}_2$  was obtained in the presence and absence of  $40 \times 10^{-3}$  M benzyl alcohol in 1 M KOH solution, as shown in Fig. 3c. Interestingly, once benzyl alcohol was added to the reaction system, the current density and anodic oxidation peak significantly increased. The CV results before and after the addition of  $40 \times 10^{-3}$  M benzyl alcohol are displayed in the inset of Fig. 3c. A noticeable positive shift value of the anodic oxidation peak is 0.05 V and an increase in the peak current could be observed after the addition of benzyl alcohol. These results reveal that the ECO of benzyl alcohol was dramatically much easier over 1.0  $\text{h-Ni(OH)}_2$  than the OER. Oxygen vacancies as active sites could provide the optimal adsorption energy to benzyl alcohol and promote the ECO process. Moreover, Fig. S20a<sup>†</sup> shows the CV curves of 1.0  $\text{h-Ni(OH)}_2$  from 1.03–1.83 V at various potential sweep rates of  $10$ – $50 \text{ mV s}^{-1}$  in 1 M KOH solution. The anodic and cathodic peak potentials shifted toward more positive and negative directions, respectively, with increasing scan rate. Fig. S20b<sup>†</sup> shows that the anodic peak current density ( $I$ ) in Fig. S20a<sup>†</sup> has a linear relationship with the scan rate ( $V$ ), thereby indicating that the ECO of benzyl alcohol is controlled by adsorption.

The concentration profiles of the reactant and products were changed at different reaction times over 1.0  $\text{h-Ni(OH)}_2$  to explore the ECO of benzyl alcohol under a continuous current (Fig. 3d). The results indicate that benzoic acid, which is stable, is the final product and that the concentration of benzoic acid increases with time. Benzaldehyde is the intermediate product, and its concentration initially increases and then decreases after peaking during electrolysis. To compare the electrocatalytic activities of samples with different Ni/Zn ratios, the ECO of benzyl alcohol was performed under similar optimal conditions using these catalysts (Fig. 3e and S21<sup>†</sup>). Among the samples tested, 1.0  $\text{h-Ni(OH)}_2$  achieved the highest conversion rate (99.99%) and selectivity (99.30%) for the ECO of benzoic acid; these values are higher than those of 0.5  $\text{h-Ni(OH)}_2$  (98.71% and 73.34%), 0.75  $\text{h-Ni(OH)}_2$  (99.55% and 83.95%), 1.25  $\text{h-Ni(OH)}_2$  (99.42% and 93.73%), and 1.5  $\text{h-Ni(OH)}_2$  (98.18% and 92.94%). The FE of each catalyst for the ECO process was calculated. The 1.0  $\text{h-Ni(OH)}_2$  revealed an FE of 98.62%, which is much higher than those of the other samples. These results indicate that conversion, selectivity, and FE are significantly influenced by the Ni/Zn ratio and the oxygen vacancies can promote ECO. We also increased the

benzyl alcohol concentration ( $40 \times 10^{-2}$  M) to view the potential for industrial implementation; benzyl alcohol is still completely converted at a current density of 200 mA, with 99.5% conversion and 99.1% selectivity in 130 min (Fig. S22†). In addition, the ECO performance of the catalysts for benzyl alcohol is consistent with the redox peak observed in Fig. 3b. When Zn is not removed from 1.0 NiZn(OH)<sub>2</sub>, 1.0 NiZn(OH)<sub>2</sub> exhibits lower conversion (95.39%), selectivity (87.97%) and FE (88.62%) compared with those of 1.0 h-Ni(OH)<sub>2</sub> under the same conditions (Fig. S23†). This observation verifies that holes and oxygen vacancies could promote the electrocatalytic ECO activity of the catalysts. 1.0 h-Ni(OH)<sub>2</sub> showed high stability in 1 M KOH and could be recycled for up to 10 consecutive catalytic runs. Its conversion rate (>99%) remained constant and its selectivity and FE for benzoic acid were >92% and >95%, respectively (Fig. 3f). The TEM and SEM (Fig. S24†) images of 1.0 h-Ni(OH)<sub>2</sub> showed no obvious change after the recycling experiments, which means the catalyst could be a stable electrocatalyst for the ECO of benzyl alcohol. A comparison of 1.0 h-Ni(OH)<sub>2</sub> and other electrocatalysts for the ECO of benzyl alcohol to benzoic acid is shown in Table S3.† In order to further explore the applications of 1.0 h-Ni(OH)<sub>2</sub>, its performance in the ECO of a series of alcohols was tested (Table 1). Good-to-excellent product yields were obtained for the oxidation of different kinds of alcohols to their corresponding acids. In most cases, the catalyst could achieve >90% conversion and >90% selectivity for the acid within ≤200 min. The excellent conversion and selectivity of 1.0 h-Ni(OH)<sub>2</sub> may be due to the presence of abundant holes and oxygen vacancies, which promote the O–H cleavage of alcohols and accelerate the ECO process.

Selective ECO of benzyl alcohols to benzaldehydes is a very important reaction in the pharmaceutical and fine chemicals industries. Herein, we employed TEMPO in the anode to determine its effect on the selective ECO of benzyl alcohol over 1.0 h-Ni(OH)<sub>2</sub> (Fig. 4a). A high anodic oxidation peak and an early initial potential of 1.0 h-Ni(OH)<sub>2</sub> could be observed during ECO after the introduction of TEMPO and benzyl alcohol. The conversion of benzyl alcohol (92.0%), the product

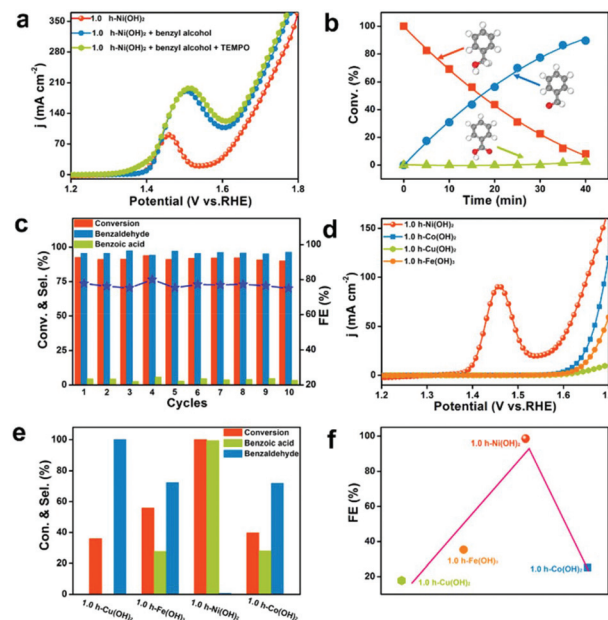


**Fig. 4** (a) LSV polarization curves of 1.0 h-Ni(OH)<sub>2</sub> in 1.0 M KOH in the absence and presence of  $40 \times 10^{-3}$  M benzyl alcohol and TEMPO. (b) Conversion and selectivity during ECO at a constant current of 20 mA in 1.0 M KOH with TEMPO and  $20 \times 10^{-3}$  M benzyl alcohol. (c) ECO conversion, selectivity, and FE of 1.0 h-Ni(OH)<sub>2</sub> after 10 successive cycles with TEMPO. (d) OER LSV curves of 1.0 h-Ni(OH)<sub>2</sub>, 1.0 h-Co(OH)<sub>2</sub>, 1.0 h-Cu(OH)<sub>2</sub>, and 1.0 h-Fe(OH)<sub>2</sub>. (e) ECO conversion and selectivity of different electrocatalysts. (f) ECO FE of different electrocatalysts.

profiles of benzaldehyde (97.45%), and the FE (75.86%) obtained under a constant current of 20 mA are presented in Fig. 4b and S25.† The results demonstrate that TEMPO can facilitate the selective ECO of benzyl alcohol to produce benzaldehyde within a specified time. As depicted in Fig. 4c, 1.0 h-Ni(OH)<sub>2</sub> displays notably high activity after 10 consecutive catalytic cycles without significant loss, which illustrates its robustness for the selective ECO of benzyl alcohol. We compared the electrocatalytic performance of different metal hydroxides (Fig. 4d) and found that 1.0 h-Ni(OH)<sub>2</sub> possesses

**Table 1** ECO of various alcohols by using 1.0 h-Ni(OH)<sub>2</sub>

Entry	Substrate	Product	Time (min)	Conv. (%)	Sel. (%)	FE (%)
1			135	99.4	98.6	94.1
2			135	92.3	95.1	85.8
3			150	92.7	92.1	76.4
4			200	98.8	98.5	94.9
5			135	96.5	93.2	88.8
6			130	99.9	99.3	98.6

Reaction conditions: Alcohol ( $40 \text{ mmol L}^{-1}$ ), 1.0 h-Ni(OH)<sub>2</sub> ( $0.625 \text{ mg cm}^{-2}$ ), current density of 20 mA, 1 M KOH. The products were determined by GC/MS and HPLC analysis.

much better OER performance than  $\text{Fe}(\text{OH})_3$ ,  $\text{Co}(\text{OH})_2$ , or  $\text{Cu}(\text{OH})_2$ ; it also showed the best ECO performance for benzyl alcohol among these hydroxides (Fig. 4e and f).

We studied the *in situ* formation of ultrafine  $\text{PtO}_2$  nanoparticles (NPs) on  $1.0 \text{ h-Ni}(\text{OH})_2$  through a simple hydrothermal treatment ( $1.0 \text{ PtO}_2/\text{h-Ni}(\text{OH})_2$ ) to investigate the electrocatalytic performance of the system in the hydrogen evolution reaction (HER). In Fig. S26,<sup>†</sup> the TEM image of  $1.0 \text{ PtO}_2/\text{h-Ni}(\text{OH})_2$  proves that  $\text{PtO}_2$  NPs were successfully loaded on  $\text{h-Ni}(\text{OH})_2$ . Fig. S27a<sup>†</sup> shows the excellent HER activity of  $1.0 \text{ PtO}_2/\text{h-Ni}(\text{OH})_2$ , which only required an overpotential of 61 mV to reach  $10 \text{ mA cm}^{-2}$ . The CF and  $1.0 \text{ h-Ni}(\text{OH})_2$  delivered the required current densities of 604 and 511 mV (Fig. S27b<sup>†</sup>), respectively. The outstanding HER performance of the  $1.0 \text{ PtO}_2/\text{h-Ni}(\text{OH})_2$  electrode was supported by the Tafel plots obtained from the related LSVs (Fig. S27c<sup>†</sup>). The Tafel slope of  $1.0 \text{ PtO}_2/\text{h-Ni}(\text{OH})_2$  ( $67 \text{ mV dec}^{-1}$ ) was much lower than those of CF ( $425 \text{ mV dec}^{-1}$ ) and  $1.0 \text{ h-Ni}(\text{OH})_2$  ( $246 \text{ mV dec}^{-1}$ ). The FE of  $1.0 \text{ PtO}_2/\text{h-Ni}(\text{OH})_2$  during the HER was determined through chronoamperometry over a period of 2120 s. In Fig. S27d,<sup>†</sup> the measured amount of  $\text{H}_2$  obtained is very consistent with the theoretical value calculated based on the transferred charge, resulting in a high FE of 97.8%. The stability of  $1.0 \text{ PtO}_2/\text{h-Ni}(\text{OH})_2$  for the HER was investigated in Fig. S28,<sup>†</sup> and only slight degradation could be observed. These results reveal that  $1.0 \text{ PtO}_2/\text{h-Ni}(\text{OH})_2$ , which features an interfacial synergy between that of  $\text{PtO}_2$  and  $\text{h-Ni}(\text{OH})_2$ , possesses excellent HER activity.

According to the above analysis, a two compartment H cell was employed to be utilized for the ECO reaction of benzyl alcohol and HER, equipped with  $1.0 \text{ h-Ni}(\text{OH})_2$  and  $1.0 \text{ PtO}_2/\text{h-Ni}(\text{OH})_2$  for the anode and cathode, respectively (Fig. 5a). Electrolysis of  $1.0 \text{ PtO}_2/\text{h-Ni}(\text{OH})_2$  and  $1.0 \text{ h-Ni}(\text{OH})_2$  yielded an overall water-splitting (OWP) current density of  $10 \text{ mA cm}^{-2}$  at 1.68 V. The electrocatalytic performance was improved when  $40 \times 10^{-3} \text{ M}$  benzyl alcohol was added to the reaction system to obtain a current density of  $10 \text{ mA cm}^{-2}$  at 1.48 V (Fig. 5b). More importantly, the FE could reach as high as 192.9%. In addition, once TEMPO was added to the reaction system, the  $10 \text{ mA cm}^{-2}$  current density point shifted further toward 1.41 V. This result indicates that the addition of TEMPO is an effective strategy to save energy when replacing the OER with the selective ECO of benzyl alcohol and that  $1.0 \text{ h-Ni}(\text{OH})_2$  may be an ideal ECO electrocatalyst. To obtain a potential approach for practical application, a paired electrolysis system equipped with  $1.0 \text{ h-Ni}(\text{OH})_2$  and  $1.0 \text{ PtO}_2/\text{h-Ni}(\text{OH})_2$  for the anode and cathode, respectively, was employed for the simultaneous ECO of benzyl alcohol and HER (Fig. 5c and S29<sup>†</sup>). A representative photograph of the electrolyzer (Fig. 5d) and the electrolytes containing the benzoic acid or benzaldehyde products are shown in Fig. 5e, indicating its great potential for implementation at a scale with industrial practicability.

To reveal the role of oxygen vacancies in  $\text{h-Ni}(\text{OH})_2$  in the ECO of benzyl alcohol, DFT calculations were used to investigate the adsorption of benzyl alcohol on vacancy-free  $\text{Ni}(\text{OH})_2$  and vacancy-rich  $\text{Ni}(\text{OH})_2$  ( $\text{V}_\text{O}\text{-Ni}(\text{OH})_2$ ). In Fig. 6a and b, the

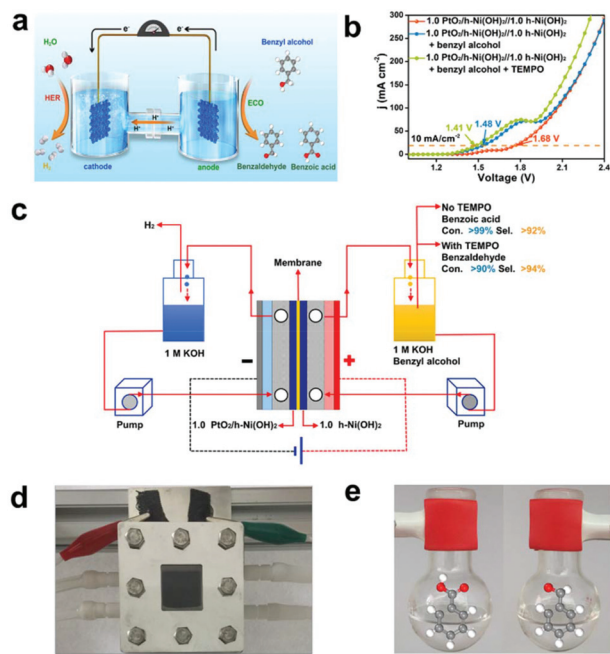
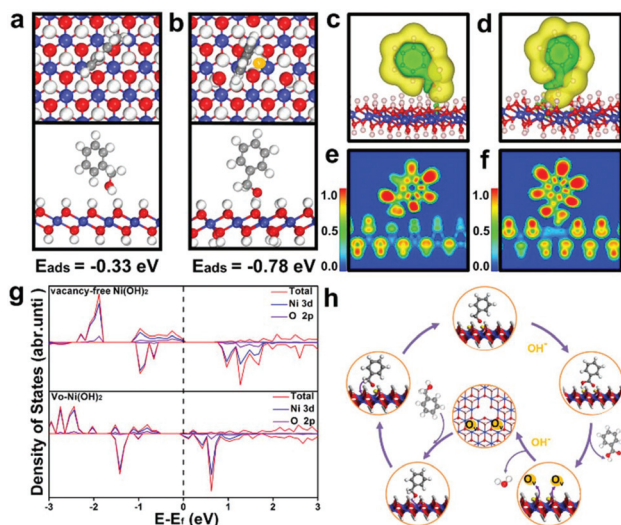


Fig. 5 (a) Schematic of the ECO of benzyl alcohol and HER equipped with  $1.0 \text{ h-Ni}(\text{OH})_2$  and  $1.0 \text{ PtO}_2/\text{h-Ni}(\text{OH})_2$ , respectively. (b) LSV curves of  $1.0 \text{ h-Ni}(\text{OH})_2$  and  $1.0 \text{ PtO}_2/\text{h-Ni}(\text{OH})_2$  electrocatalysts in the absence and presence of  $40 \times 10^{-3} \text{ M}$  benzyl alcohol and TEMPO. (c) Schematic of the paired electrolysis system. (d) Photograph of the electrolyzer for the ECO of benzyl alcohol and HER. Here,  $1.0 \text{ h-Ni}(\text{OH})_2$  (right) and  $1.0 \text{ PtO}_2/\text{h-Ni}(\text{OH})_2$  (left) are used as electrocatalysts. (e) Photograph of the product for the ECO of benzyl alcohol.

adsorption of benzyl alcohol on vacancy-free  $\text{Ni}(\text{OH})_2$  is only  $-0.33 \text{ eV}$ , thus implying that benzyl alcohol forms a weak interaction. When  $\text{V}_\text{O}\text{-Ni}(\text{OH})_2$  is employed, the adsorption energies of benzyl alcohol increase to  $-0.78 \text{ eV}$ , which is much stronger than that on vacancy-free  $\text{Ni}(\text{OH})_2$ , consistent with previous studies.<sup>70,71</sup> Meanwhile, the oxygen atom in benzyl alcohol obtains more charges on  $\text{V}_\text{O}\text{-Ni}(\text{OH})_2$  than on vacancy-free  $\text{Ni}(\text{OH})_2$  (Table S4<sup>†</sup>). These results indicate that oxygen vacancies enhance the adsorption energy of benzyl alcohol. The analysis results of charge density differences agree well with the Bader charge (Fig. 6c and d). The electron localization functions (ELFs) of benzyl alcohol on  $\text{V}_\text{O}\text{-Ni}(\text{OH})_2$  and vacancy-free  $\text{Ni}(\text{OH})_2$  were analyzed in Fig. 6e and f, and a much stronger interaction between benzyl alcohol and  $\text{V}_\text{O}\text{-Ni}(\text{OH})_2$  than that between benzyl alcohol and vacancy-free  $\text{Ni}(\text{OH})_2$  was observed. Furthermore, the electronic structure of vacancy-free  $\text{Ni}(\text{OH})_2$  and  $\text{V}_\text{O}\text{-Ni}(\text{OH})_2$  has been further studied. As shown by the density of states (DOS) in Fig. 6g, compared to the vacancy-free  $\text{Ni}(\text{OH})_2$ , the Fermi surface of  $\text{V}_\text{O}\text{-Ni}(\text{OH})_2$  apparently transfers to the conduction band edge, which confirms that the conduction band minimum of  $\text{V}_\text{O}\text{-Ni}(\text{OH})_2$  can obtain more carriers.<sup>72</sup> This result manifested that the DOS on the Fermi surface of vacancy-free  $\text{Ni}(\text{OH})_2$  increases significantly, demonstrating that  $\text{V}_\text{O}\text{-Ni}(\text{OH})_2$  possesses higher conductivity and carrier density to facilitate electron transfer during the ECO process.<sup>73</sup> In general, the DFT calculations revealed that



**Fig. 6** DFT-calculated adsorption energies of benzyl alcohol on (a) vacancy-free Ni(OH)<sub>2</sub> and (b) oxygen vacancies (V<sub>O</sub>-Ni(OH)<sub>2</sub>); the charge density difference of benzyl alcohol on (c) vacancy-free Ni(OH)<sub>2</sub> and (d) oxygen vacancies (V<sub>O</sub>-Ni(OH)<sub>2</sub>), negative and positive charges are presented in green and yellow, respectively; the ELF of benzyl alcohol on (e) vacancy-free Ni(OH)<sub>2</sub> and (f) oxygen vacancies (V<sub>O</sub>-Ni(OH)<sub>2</sub>). The ELF value is set in the range of 0–1, where 1, 0.5, and 0 respectively represent covalent, metallic, and no-bonding characteristics; and (g) the density of states (DOS) of vacancy-free Ni(OH)<sub>2</sub> and oxygen vacancies (V<sub>O</sub>-Ni(OH)<sub>2</sub>). (h) Reaction pathways for the ECO of benzyl alcohol with 1.0 h-Ni(OH)<sub>2</sub> as the electrocatalyst. Navy, red and gray colors stand for Ni, O, and C atoms respectively, and white and yellow colors stand for H atoms.

the unique defective structure of V<sub>O</sub>-Ni(OH)<sub>2</sub> plays a vital role in influencing the adsorption energy of benzyl alcohol, thus facilitating the entire ECO process and enhancing the electrocatalytic activity of the nanohybrids.

Based on the above results and previous studies,<sup>74,75</sup> a possible reaction pathway to form benzoic acid over 1.0 h-Ni(OH)<sub>2</sub> can be proposed as in Fig. 6h. Firstly, benzyl alcohol could be adsorbed on oxygen vacancies, and its hydroxyl radical may be activated. This reaction results in deprotonation and formation of an alkoxy intermediate, which becomes a higher valence oxide Ni<sup>3+</sup>=O in an alkaline solution. Subsequently, the redox couple Ni<sup>3+</sup>=O/Ni<sup>2+</sup>=O of the active electrocatalyst surface subjects the alkoxy intermediate to C–H bond cleavage to form the benzaldehyde. Afterward, the benzaldehyde species –CHO combines with OH<sup>–</sup> from the solution to form a –CHOH<sup>–</sup> species. Finally, Ni<sup>3+</sup>=O further interacts with –CHOH<sup>–</sup> species by electron transfer to form benzoic acid and produce Ni<sup>2+</sup>=O, followed by reaction with hydroxide ions to complete the electrocatalytic cycle.

## Conclusions

In this work, *in situ* loading of 1.0 h-Ni(OH)<sub>2</sub> on CF was performed. The Ostwald ripening process introduced highly dense holes and oxygen vacancies on the surface of

1.0 h-Ni(OH)<sub>2</sub>, and the prepared electrode exhibited remarkable electrocatalytic performance with superior activity and prominent durability for OER; the catalyst was also successfully applied to the selective ECO of benzyl alcohol in an alkaline medium under optimal reaction conditions, as well as to the simultaneous selective ECO of benzyl alcohol and H<sub>2</sub> production with a high FE in a paired electrolysis system. By virtue of the high uniform orientation of nanosheets, the abundant holes and oxygen vacancies in h-Ni(OH)<sub>2</sub> provide a highly exposed surface area and an abundance of active sites, which are beneficial for mass transfer and improve the electrocatalytic reaction. DFT calculations confirmed that the formation of oxygen vacancies increases the charge transfer between V<sub>O</sub>-Ni(OH)<sub>2</sub> and benzyl alcohol, thus facilitating increases in adsorption capability toward benzyl alcohol and promoting ECO. The proposed strategy offers new opportunities to develop defective electrocatalysts for the green chemical industry and energy conversion.

## Conflicts of interest

There are no conflicts to declare.

## Acknowledgements

The authors acknowledge the financial support from the National Natural Science Foundation of China (NSFC-21625604, 21776251, 21878272 and 21671172).

## Notes and references

- W. Zhong, H. Liu, C. Bai, S. Liao and Y. Li, *ACS Catal.*, 2017, **5**, 1417–1426.
- H. G. Cha and K. S. Choi, *Nat. Chem.*, 2015, **7**, 328–333.
- D. P. Hickey, M. S. Mccammant, F. Giroud, M. S. Sigman and S. D. Minter, *J. Am. Chem. Soc.*, 2014, **136**, 15917–15920.
- M. Trincado and D. Banerjee, *Energy Environ. Sci.*, 2014, **7**, 2464–2503.
- N. Kakati, J. Maiti, S. H. Lee, S. H. Jee, B. Viswanathan and Y. S. Yoon, *Chem. Rev.*, 2014, **114**, 12397–12429.
- Q. Wang, L. Chen, S. Guan, X. Zhang, B. Wang, X. Cao, Z. Yu, Y. He, D. G. Evans and J. Feng, *ACS Catal.*, 2018, **8**, 3104–3115.
- X. Xiao, C. Zheng, M. Lu, L. Zhang, F. Liu, X. Zuo and J. Nan, *Appl. Catal., B*, 2018, **228**, 142–151.
- S. D. Mccann and S. S. Stahl, *Acc. Chem. Res.*, 2015, **46**, 1756–1766.
- J. M. Hoover, B. L. Ryland and S. S. Stahl, *ACS Catal.*, 2016, **3**, 2599–2605.
- Z. Zhang and G. W. Huber, *Chem. Soc. Rev.*, 2018, **47**, 1351–1390.
- P. Zhang, Y. Gong, H. Li, Z. Chen and Y. Wang, *Nat. Commun.*, 2013, **4**, 1593.

- 12 Y. Su, Z. Han, L. Zhang, W. Wang, M. Duan, X. Li, Y. Zheng, Y. Wang and X. Lei, *Appl. Catal., B*, 2017, **217**, 108–114.
- 13 J. I. Kroschwitz, *Kirk-Othmer Encycl. Chem. Technol.*, 1992, **4**, 64–72.
- 14 J. A. B. Satrio and L. K. Doraiswamy, *Chem. Eng. J.*, 2001, **82**, 43–56.
- 15 M. J. Lima, A. M. T. Silva, C. G. Silva and J. L. Faria, *J. Catal.*, 2017, **353**, 44–53.
- 16 M. L. Kantam, B. M. Choudary, P. Sreekanth, K. K. Rao, K. Naik, T. P. Kumar and A. A. Khan, *US Pat.*, 6495726, 2002.
- 17 B. You and Y. Sun, *Acc. Chem. Res.*, 2018, **51**, 1571–1580.
- 18 B. You, X. Liu, N. Jiang and Y. Sun, *J. Am. Chem. Soc.*, 2016, **138**, 13639–13646.
- 19 B. You, N. Jiang, X. Liu and Y. Sun, *Angew. Chem., Int. Ed.*, 2016, **55**, 9913–9917.
- 20 E. J. Horn, B. R. Rosen, Y. Chen, J. Tang, K. Chen, M. D. Eastgate and P. S. Baran, *Nature*, 2016, **533**, 77–81.
- 21 R. Francke and R. D. Little, *Chem. Soc. Rev.*, 2014, **43**, 2492–2521.
- 22 A. Badalyan and S. S. Stahl, *Nature*, 2016, **535**, 406.
- 23 S. Yamazaki, M. Yao, N. Fujiwara, Z. Siroma, K. Yasuda and T. Ioroi, *Chem. Commun.*, 2012, **48**, 4353–4355.
- 24 M. Yasuzawa, K. Kan, A. Kunugi, Z. Ogumi and Z. I. Takehara, *Electrochim. Acta*, 1995, **40**, 1785–1787.
- 25 A. L. B. Marques, W. Li, E. P. Marques and J. Zhang, *Electrochim. Acta*, 2004, **49**, 879–885.
- 26 M. Rafiee, K. C. Miles and S. S. Stahl, *J. Am. Chem. Soc.*, 2015, **137**, 14751.
- 27 A. Das and S. S. Stahl, *Angew. Chem., Int. Ed.*, 2017, **129**, 8892–8897.
- 28 Z. Yin, Y. Zheng, H. Wang, J. Li, Q. Zhu, Y. Wang, N. Ma, G. Hu, B. He and A. Knopgericke, *ACS Nano*, 2017, **11**, 12365–12377.
- 29 Y. Li, H. Wang, Y. Li, Q. Wang, D. Li, R. Wang, B. He and Y. Gong, *J. Catal.*, 2018, **364**, 48–56.
- 30 D. Yan, Y. Li, J. Huo, R. Chen, L. Dai and S. Wang, *Adv. Mater.*, 2017, **29**, 1606459.
- 31 G. Wang, Y. Yang, D. Han and Y. Li, *Nano Today*, 2017, **13**, 23–39.
- 32 L. Zhuang, L. Ge, Y. Yang, M. Li, Y. Jia, X. Yao and Z. Zhu, *Adv. Mater.*, 2017, **29**, 1606793.
- 33 J. Kim, X. Yin, K. C. Tsao, S. Fang and H. Yang, *J. Am. Chem. Soc.*, 2014, **136**, 14646–14649.
- 34 C. Tang and Q. Zhang, *Adv. Mater.*, 2017, **29**, 1604103.
- 35 C. Tang, H.-F. Wang and Q. Zhang, *Acc. Chem. Res.*, 2018, **51**, 881–889.
- 36 J. Yin, Y. Li, F. Lv, M. Lu, K. Sun, W. Wang, L. Wang, F. Cheng, Y. Li and P. Xi, *Adv. Mater.*, 2017, **29**, 1704681.
- 37 Z. Li, H. Duan, M. Shao, J. Li, D. O'Hare, M. Wei and Z. L. Wang, *Chem*, 2018, **4**, 2168–2179.
- 38 C. Tang, H.-F. Wang, X. Chen, B.-Q. Li, T.-Z. Hou, B. Zhang, Q. Zhang, M.-M. Titirici and F. Wei, *Adv. Mater.*, 2016, **28**, 6845–6851.
- 39 S. Wang, D. Chen, M. Qiao, Y. Lu, L. I. Hao, D. Liu, C. Dong and Y. Li, *Angew. Chem., Int. Ed.*, 2018, **130**, 8827–8832.
- 40 M. Gong, Y. Li, H. Wang, Y. Liang, J. Z. Wu, J. Zhou, J. Wang, T. Regier, F. Wei and H. Dai, *J. Am. Chem. Soc.*, 2013, **135**, 8452–8455.
- 41 X. Jia, Y. Zhao, G. Chen, L. Shang, R. Shi, X. Kang, G. I. N. Waterhouse, L. Z. Wu, C. H. Tung and T. Zhang, *Adv. Energy Mater.*, 2016, **6**, 1502585.
- 42 L. Feng, F. Song and X. Hu, *Energy Environ. Sci.*, 2015, **8**, 2347–2351.
- 43 H. Liang, L. Li, F. Meng, L. Dang, J. Zhuo, A. Forticaux, Z. Wang and S. Jin, *Chem. Mater.*, 2015, **27**, 5702–5711.
- 44 P. Wang, Q. Shao, X. Cui, X. Zhu and X. Huang, *Adv. Funct. Mater.*, 2017, **28**, 1705918.
- 45 R. Subbaraman and N. M. Markovic, *Science*, 2012, **43**, 1256–1260.
- 46 L. Chen, X. Dong, Y. Wang and Y. Xia, *Nat. Commun.*, 2016, **7**, 11741.
- 47 X. Kong, C. Zhang, Y. H. Sang, Q. Chen and Z. Peng, *Small*, 2017, **13**, 1700334.
- 48 J. Xie, X. Zhang, H. Zhang, J. Zhang, S. Li, R. Wang, B. Pan and Y. Xie, *Adv. Mater.*, 2017, **29**, 1604765.
- 49 G. Kresse and J. Furthmuller, *Phys. Rev. B: Condens. Matter Mater. Phys.*, 1996, **54**, 11169–11186.
- 50 G. Kresse and J. Furthmuller, *Comput. Mater. Sci.*, 1996, **6**, 15–50.
- 51 G. Kresse and J. Hafner, *Phys. Rev. B: Condens. Matter Mater. Phys.*, 1994, **49**, 14251–14269.
- 52 G. Kresse and D. Joubert, *Phys. Rev. B: Condens. Matter Mater. Phys.*, 1999, **59**, 1758–1775.
- 53 J. P. Perdew, K. Burke and M. Ernzerhof, *Phys. Rev. Lett.*, 1996, **77**, 3865–3868.
- 54 P. E. Blochl, *Phys. Rev. B: Condens. Matter Mater. Phys.*, 1994, **50**, 17953–17979.
- 55 B. Mao, D. Guo, J. Qin, T. Meng, X. Wang and M. Cao, *Angew. Chem., Int. Ed.*, 2017, **57**, 446–450.
- 56 M. Gao, W. Sheng, Z. Zhuang, Q. Fang, S. Gu, J. Jiang and Y. Yan, *J. Am. Chem. Soc.*, 2014, **136**, 7077–7084.
- 57 B. Liu and H. C. Zeng, *Small*, 2005, **1**, 566–571.
- 58 W. Ostwald, *Lehrbuch der Allgemeinen Chemie*, Engelmann, Leipzig, Germany, 1898.
- 59 S. K. Mazloomi and N. Sulaiman, *Renewable Sustainable Energy Rev.*, 2012, **16**, 4257–4263.
- 60 Z. Lu, W. Zhu, X. Yu, H. Zhang, Y. Li, X. Sun, X. Wang, H. Wang, J. Wang and J. Luo, *Adv. Mater.*, 2014, **26**, 2683–2687.
- 61 X. Yu, P. Yang, S. Chen, M. Zhang and G. Shi, *Adv. Energy Mater.*, 2017, **7**, 1601805.
- 62 X. Yu, J. Zhao, L. R. Zheng, Y. Tong, M. Zhang, G. Xu, C. Li, J. Ma and G. Shi, *ACS Energy Lett.*, 2017, **3**, 237–244.
- 63 Z. Zeng, K. C. Chang, J. Kubal, N. M. Markovic and J. Greeley, *Nature*, 2017, **2**, 17070.
- 64 Z. Chen, C. Kronawitter, Y. W. Yeh, X. Yang, P. Zhao, N. Yao and B. Koel, *J. Mater. Chem. A*, 2016, **5**, 842–850.
- 65 J. Wang, J. Liu, B. Zhang, H. Wan, Z. Li, X. Ji, K. Xu, C. Chen, D. Zha and L. Miao, *Nano Energy*, 2017, **42**, 98–105.
- 66 C. Luan, G. Liu, Y. Liu, L. Yu, Y. Wang, Y. Xiao, H. Qiao, X. Dai and X. Zhang, *ACS Nano*, 2018, **12**, 3875–3885.

- 67 K. Xu, P. Chen, X. Li, Y. Tong, H. Ding, X. Wu, W. Chu, Z. Peng, C. Wu and Y. Xie, *J. Am. Chem. Soc.*, 2015, **137**, 4119–4125.
- 68 M. Gong and H. Dai, *Nano Res.*, 2014, **8**, 23–39.
- 69 M. W. Louie and A. T. Bell, *J. Am. Chem. Soc.*, 2013, **135**, 12329–12337.
- 70 Y. Du, Q. Wang, X. Liang, Y. He, J. Feng and D. Li, *J. Catal.*, 2015, **331**, 154–161.
- 71 Z. Zhang, O. Bondarchuk, J. M. White, B. D. Kay and Z. Dohnalek, *J. Am. Chem. Soc.*, 2006, **128**, 4198–4199.
- 72 T. Ling, D. Y. Yan, Y. Jiao, H. Wang, Y. Zheng, X. Zheng, J. Mao, X. W. Du, Z. Hu and M. Jaroniec, *Nat. Commun.*, 2016, **7**, 12876.
- 73 Y. Tong, P. Chen, M. Zhang, T. Zhou, L. Zhang, W. Chu, C. Wu and Y. Xie, *ACS Catal.*, 2017, **8**, 1–7.
- 74 A. Abad, P. Concepción, A. Corma and H. García, *Angew. Chem., Int. Ed.*, 2005, **117**, 4134–4137.
- 75 J. Zheng, X. Chen, X. Zhong, S. Li, T. Liu, G. Zhuang, X. Li, S. Deng, D. Mei and J. G. Wang, *Adv. Funct. Mater.*, 2017, **27**, 1704169.